Heliyon 10 (2024) e30962

Contents lists available at ScienceDirect

Heliyon

journal homepage: www.cell.com/heliyon

Research article

Physiologically based pharmacokinetic model for predicting the biodistribution of albumin nanoparticles after induction and recovery from acute lung injury

Elena O. Kutumova [a,b,c], Ilya R. Akberdin [a,c,d], Vera S. Egorova [e], Ekaterina P. Kolesova [e], Alessandro Parodi [e,*], Vadim S. Pokrovsky [f,g], Andrey A. Zamyatnin, Jr [e,h,i,**], Fedor A. Kolpakov [a,b,c]

[a] Department of Computational Biology, Sirius University of Science and Technology, 354340, Sirius, Krasnodar Region, Russia
[b] Laboratory of Bioinformatics, Federal Research Center for Information and Computational Technologies, 630090, Novosibirsk, Russia
[c] Biosoft.Ru, Ltd., 630058, Novosibirsk, Russia
[d] Department of Natural Sciences, Novosibirsk State University, 630090, Novosibirsk, Russia
[e] Scientific Center for Translational Medicine, Sirius University of Science and Technology, 354340, Sirius, Krasnodar Region, Russia
[f] N.N. Blokhin Medical Research Center of Oncology, 115522, Moscow, Russia
[g] Patrice Lumumba People's Friendship University, 117198, Moscow, Russia
[h] Faculty of Bioengineering and Bioinformatics and Belozersky Institute of Physico-Chemical Biology, Lomonosov Moscow State University, 119234, Moscow, Russia
[i] Department of Biological Chemistry, Sechenov First Moscow State Medical University, 119991, Moscow, Russia

ARTICLE INFO

Keywords:
Nanomedicine
Lipopolysaccharide injection
Murine model
Albumin nanoparticle biodistribution
PBPK modeling
BioUML
Acute lung injury

ABSTRACT

The application of nanomedicine in the treatment of acute lung injury (ALI) has great potential for the development of new therapeutic strategies. To gain insight into the kinetics of nanocarrier distribution upon time-dependent changes in tissue permeability after ALI induction in mice, we developed a physiologically based pharmacokinetic model for albumin nanoparticles (ANP). The model was calibrated using data from mice treated with intraperitoneal LPS (6 mg/kg), followed by intravenous ANP (0.5 mg/mouse or about 20.8 mg/kg) at 0.5, 6, and 24 h. The simulation results reproduced the experimental observations and indicated that the accumulation of ANP in the lungs increased, reaching a peak 6 h after LPS injury, whereas it decreased in the liver, kidney, and spleen. The model predicted that LPS caused an immediate (within the first 30 min) dramatic increase in lung and kidney tissue permeability, whereas splenic tissue permeability gradually increased over 24 h after LPS injection. This information can be used to design new therapies targeting specific organs affected by bacterial infections and potentially by other inflammatory insults.

* Corresponding author. Scientific Center for Translational Medicine, Sirius University of Science and Technology, Olympic Ave, 1, Bolshoy Sochi, Krasnodar Krai, 354340, Sirius, Krasnodar Region, Russia

** Corresponding author. Faculty of Bioengineering and Bioinformatics, Lomonosov Moscow State University, Leninskie gory 1-73, 119234, Moscow, Russia

E-mail addresses: parodi.a@talantiuspeh.ru (A. Parodi), zamyat@belozersky.msu.ru (A.A. Zamyatnin, Jr).

https://doi.org/10.1016/j.heliyon.2024.e30962
Received 24 October 2023; Received in revised form 2 April 2024; Accepted 8 May 2024
Available online 10 May 2024

1. Introduction

Acute lung injury (ALI) is a severe clinical syndrome that, at the most critical stage of the disease spectrum, can cause acute respiratory distress syndrome (ARDS) [1–5]. The common causes of ALI are sepsis [6–9], pneumonia [10,11], trauma [12–16], aspiration [17–19], inhalation of toxic molecules [20–24], treatment-related adverse effects [25,26], and pancreatitis [27–29]. Despite advances in critical care, there is currently no effective medication targeting the underlying pathophysiology of ALI, and management of this disease remains supportive, mostly focusing on addressing the inciting cause [30]. The limited success of pharmacological therapies has led to the development of new agents, such as innovative nanomedicine approaches, specifically aimed at treating ALI [31–35].

Human clinical studies have provided information on the onset and evolution of physiological and inflammatory changes in the lungs. However, further characterization of the mechanisms of injury in humans is complicated by many clinical variables that are difficult to control in critically ill patients [36].

Acute lung inflammation can be induced in mice by administering lipopolysaccharide (LPS) through various routes including direct delivery into the upper and lower airways [37–41], intravenous [42–45] and intraperitoneal [46–49] injection, or by spraying it all over the body [50]. In order to design and customize targeted anti-inflammatory treatments, it is important to investigate the biodistribution of nanoparticles in LPS-induced ALI. However, considering the wide range of delivery platforms available, it is necessary to conduct this investigation for all nanocarriers [51–56]. In this regard, physiologically based pharmacokinetic (PBPK) modeling can expedite the process by providing valuable predictions and mechanistic insights into the effectiveness and potential toxicity of nanocarriers [57–59]. In this effort, it is crucial to consider that acute lung injury occurs with specific kinetics and potency depending on the concentration of LPS used. It is worth noting that if the administration of LPS does not lead to a lethal outcome, this phenomenon is reversible.

PBPK models typically consist of multiple compartments, each representing distinct body regions, such as a group of organs/tissues (e.g., rapidly/slowly perfused tissues) [60] or a single organ/tissue (e.g., lungs, liver, kidneys, etc.) [61–63]. To date, dozens of models have been developed to analyze the biodistribution of inorganic nanomaterials (including iron, gold, silver, platinum, and silica) [57]. In this context, the number of models designed for organic/biological nanoparticles is very modest [64–68], while models adapted for albumin nanoparticles are even fewer [69]. Also, nanomedicine was developed primarily for cancer disease, while other pathological conditions, including ALI, were not extensively considered.

The objective of this study was to create a PBPK model to accurately depict the evolving biodistribution of nanoparticles following mild ALI induction and recovery while examining alterations in tissue permeability through a numerical analysis of the process. To accomplish this, we chose albumin nanoparticles (ANP) as a nanodelivery platform owing to their extensive use, biocompatibility, natural ability to transport drugs, and cost-effectiveness in drug delivery applications, including ALI [70–72]. In this study, we simulated the accumulation of particles within the lungs and their clearance from this organ at various time intervals following both LPS injection and particle administration. We demonstrated that the clearance of particles from the lungs depended on the time at which LPS was injected. Specifically, we found that maximal accumulation in the lungs occurred within 6 h of LPS injection, with a decrease observed at 24 h. This study contributes to the broader field of particle biodistribution science, which typically focuses on cancer diseases.

2. Materials and methods

2.1. Albumin nanoparticle synthesis and characterization

Albumin nanoparticles were synthesized by desolvation followed by cross-linking method as shown by Kolesova et al. [73]. Protein denaturation and nanoparticle formation occurred by adding ethanol dropwise at room temperature to a water solution of bovine serum albumin (20 mg/mL) in a ratio ethanol/water 4 of 1. Ethanol was added with constant stirring at a speed (2 mL/min) using a digital pump system (Masterflex L/S). Subsequently, 40 μL glutaraldehyde (25 % solution) dissolved in 1 mL of ethanol was added dropwise. The resulting solution was then stirred overnight at room temperature. The day after the particles were centrifuged at 13, 000 RPM, the supernatant was discarded, and the particles were washed in MQ water several times. Particle concentration was determined by drying a known volume of particles at 65 °C overnight and weighing the pellet.

2.2. Nanoparticle size and surface charge characterization

The ζ potential and size distribution measurements were performed using a Zetasizer Nano ZS automatic analyzer (Malvern Instruments, UK) at 25 °C. A buffer at physiological pH was used to prepare nanoparticle dispersions for the dynamic light scattering (DLS) measurements. Prior to the DLS analysis, the nanoparticles were dispersed in a buffer solution and sonicated for 5 min at room temperature. Intensity, number, and volume size distributions were used for the analysis (particle concentration = 5 mg/mL). ζ-Potential measurements were performed using the Smoluchowski model.

2.3. Albumin nanoparticle toxicity in vitro

The impact of nanoparticles on cell viability was evaluated via MTT as shown in Ref. [74]. In brief the cells were seeded in 96-well microplates (Costar, 158 Corning Inc., Corning, NY) at a density of 10^4. Twenty-four hours after cell attachment, plates were washed

with PBS, and cells were treated with increasing concentrations, from 2 to 20 ng/cell (or 100–1000 μg/mL), of albumin nanoparticles (ANP) for 6 h, and then washed, and cultured for an additional 66 h. Six replicate wells were used for each of the control and tested concentrations. The tetrazolium salt (MTT [3-(4,5–164 dimethylthiazol-2-yl)-2,5-diphenyltetrazolium bromide]) was dissolved in PBS (5 mg/mL) and added to differentiated macrophages (100 μL/mL DMEM without serum or phenol red). After incubation for 3 h at 37 °C, a solution of isopropanol was pipetted into each well and mixed to dissolve the dark blue formazan crystals that formed. After incubation for a few minutes at room temperature, the absorbance of the plates was read at 570 nm using a BioTek Microplate reader.

2.4. *In vivo imaging system (IVIS) analysis of nanoparticle biodistribution*

Animal studies were approved by the N.N. Blokhin Medical Research Center of Oncology, ethical committee (Protocol Number 08P-13.12.2022). Non-lethal ALI was induced in male BALB/c mice (6-8 week-old) by intraperitoneal (i. p.) injection of LPS (6 mg/kg, 200 μl per mouse following the procedure shown in Ref. [75] and slightly adjusted for the mouse strain). Mice were intravenously injected with fluorescently labeled ANP (0.5 mg/mouse or about 20.8 mg/kg; $n = 3$ per time point of particle distribution, per time point of particle administration after LPS injection. CTRL mice were injected only with the particles. Total injection volume 100 μl; total number of mice = 60) at different time points after LPS administration (0.5, 6, and 24 h). At different time points after particle

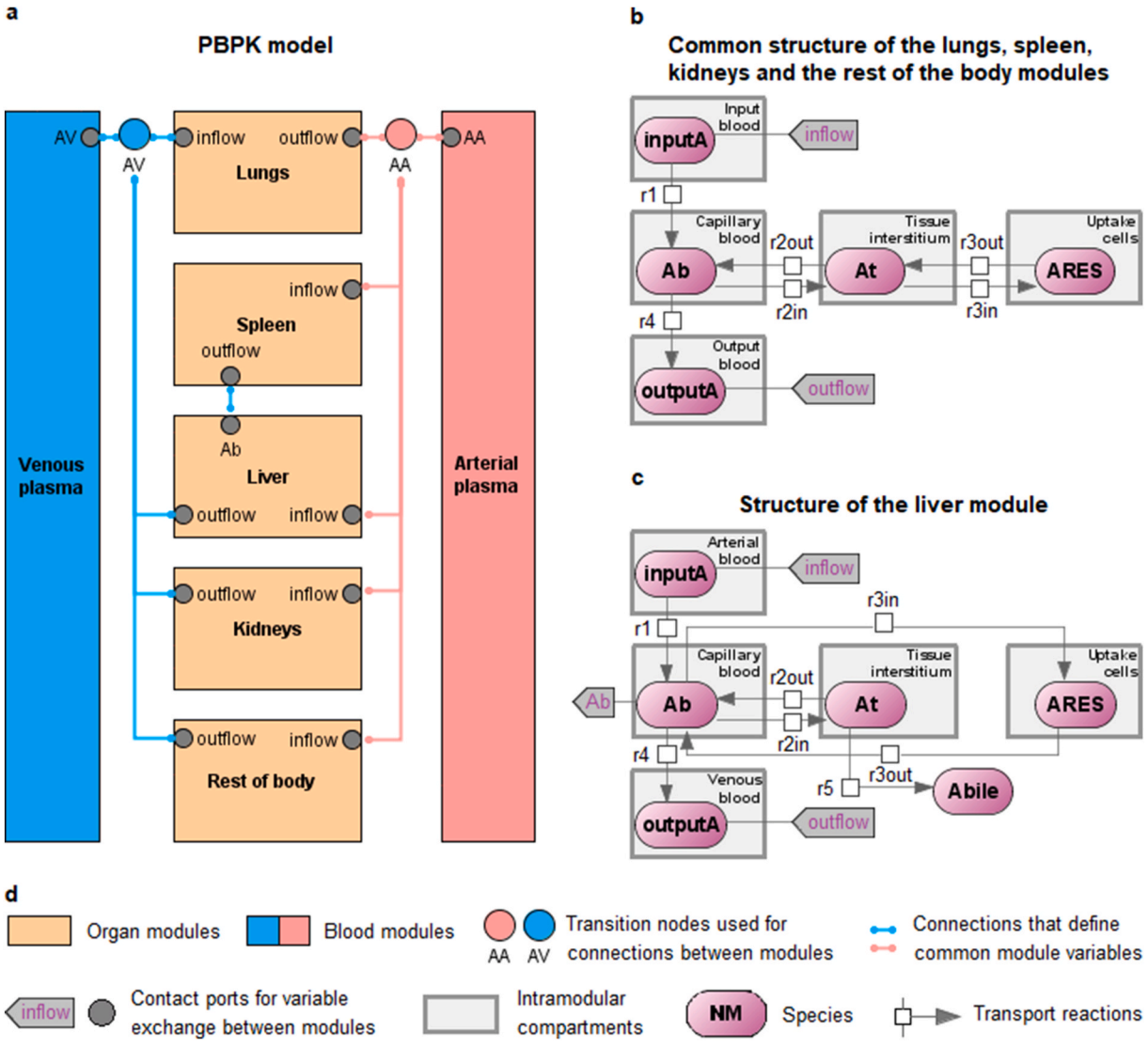

Fig. 1. Schematic representation of the modular computational PBPK model of ANP biodistribution in mice. (**a**) The model comprises arterial (red) and venous (blue) blood flows (with ANP amounts of *AA* and *AV*, respectively), four organ compartments of the mononuclear phagocyte system (lungs, spleen, liver, kidneys), and a rest of the body compartment. (**b**) The common structure of the lungs, spleen, kidneys, and the rest of the body modules. (**c**) Determination of the liver module. (**d**) Graphical notation used to represent the model.

administration (10, 180, 360, 1440, and 2880 min), three mice were sacrificed via cervical dislocation. The lungs, liver, spleen, and kidneys were analyzed using IVIS (PerkinElmer) for their total radiant efficiency, and the data were normalized against organ area. All animal studies were conducted in accordance with the Decision No 81 of Council of the Eurasian Economic Commission "On approval of rules of good laboratory practice of the Eurasian Economic Union in the sphere of circulation of medicines" issued on November 3, 2016 and Directive 2010/63/EU of European Parliament and European Counsel issued on September 22, 2010 "On the protection of animals used in the laboratory research" and were reviewed and approved by the N.N. Blokhin National Medical Research Center of Oncology Ethics Committee (No. 08p-13/12/2022 from December 13, 2022). Experiments were performed in the animal facility of N. N. Blokhin National Medical Research Center of Oncology, Moscow, Russia.

2.5. PBPK model structure

The model of albumin nanoparticle delivery (Fig. 1a) was constructed based on the modular model by Cheng et al. [69] using a visual modeling approach [76]. It included seven compartments determined as separate computational modules: arterial and venous plasma, lungs, spleen, liver, kidneys, and the remaining tissues.

According to Cheng et al. [69], the model considers the uneven distribution of injected ANP between capillary blood and organ tissue, membrane-limited transcapillary transport, nonlinear endocytic uptake, and first-order exocytic release. As nanoparticle exocytosis is a phenomenon still under debate [77–79] in terms of degree, intensity, and duration, exocytic release and removal of nanoparticles from tissue might also include a decrease in particle fluorescence, particle degradation, or clearance from the interstitial space to the lymphatic system of the carriers. Compartments representing the lungs, spleen, kidneys, and the rest of the body were designed using the same differential-algebraic equations, but with different parameter values. We isolated these equations into a separate submodule that received parameter values that were specific to each compartment. The system of these equations can be defined as a chain of irreversible (→) and reversible (↔) reactions (Fig. 1b):

$$inputA \xrightarrow{r1} Ab; \quad Ab \xleftrightarrow[r2in,r2out]{} At \xleftrightarrow[r3in,r3out]{} ARES; \quad Ab \xrightarrow{r4} outputA, \tag{1}$$

where *inputA* and *outputA* denote the amount of ANP in the input (venous for lungs and arterial for other organs) and output (arterial for lungs and venous for other organs) plasma flows, *Ab* and *At* correspond to the amount of ANP in capillary blood and tissue interstitium of organs, respectively, and *ARES* is the amount of ANP taken up from the tissue interstitium by phagocytosis.

The liver compartment cannot be expressed in terms of a general system of equations, since it contains Kupffer cells capable of nanoparticles phagocytosis directly from the capillary blood [69]. The chain of reactions in this case is as follows (Fig. 1c):

$$inputA \xrightarrow{r1} Ab; \quad Ab \xleftrightarrow[r2in,r2out]{} At; \quad Ab \xleftrightarrow[r3in,r3out]{} ARES; \quad Ab \xrightarrow{r4} outputA. \tag{2}$$

Despite the different sequences of reactions (1) and (2), the correspondipd0 reaction rates were calculated using the same kinetic laws. Appendix A provides a detailed description of all formulas. Therefore, here, we focus only on reactions whose parameters have been optimized to match the model with the experimental data describing ANP biodistribution kinetics (10–2880 min) administered at different time points (0–1440 min) after LPS injection. The diffusion of ANP through the capillary wall into the tissue interstitium (*r2in*) depends on the permeability coefficient *PAC*, regional blood flow *Q*, and capillary blood volume *Vb*, and is defined by the following formula:

$$v_2^{in} = PAC \cdot Q \cdot \frac{Ab}{Vb}. \tag{3}$$

The reverse process (*r2out*) is calculated as:

$$v_2^{out} = \frac{PAC}{P} \bullet Q \bullet \frac{At}{Vt}, \tag{4}$$

where *Vt* denotes the volume of the tissue interstitium and *P* is a constant. From a biological point of view, the process of releasing nanoparticles from the tissue back into the blood is rare. Therefore, equation (4) is used to account for the uneven distribution of nanoparticles between the interstitial fluid and plasma in each organ [63]. Speaking of experimental analogies, the *PAC* parameter can be compared with cell permeability, which is estimated from the change in transepithelial/transendothelial electrical resistance [80,81], while the *P* parameter determines the amount of accumulation of nanoparticles in the tissue [82,83]. That is, both parameters characterize the penetration of nanoparticles into the tissue, and the division of this process into two equations in the model is of a technical nature.

The rate of endocytic/phagocytic uptake of ANP (*r3in*) is described by the Hill function with the parameters *KRESmax* (maximum uptake rate), *KRES*50 (time to reach a half-maximum uptake rate), and *KRESn* (Hill coefficient):

$$v_3^{in} = KRESUP \cdot At, KRESUP = \frac{KRESmax \bullet t^{KRESn}}{KRES50^{KRESn} + t^{KRESn}}. \tag{5}$$

The rate of ANP exocytic release (*r3out*) was determined using the constant coefficient *KRESrelease* as follows:

$$v_3^{out} = KRESrelease \cdot ARES. \tag{6}$$

In addition to equations (3)–(6), the liver and kidney compartments include reactions of ANP excretion through the biliary and urinary tracts, proceeding at rates:

$$v_b = KbileC \cdot BW^{0.75} \cdot \frac{At}{Vt}, v_u = KurineC \cdot BW^{0.75} \cdot \frac{Ab}{Vb}. \quad (7)$$

Here, At/Vt and Ab/Vb define the concentration of ANP in the tissue and capillary blood of the corresponding compartment, respectively, whereas *KbileC* and *KurineC* are excretion constants.

2.6. Modeling software

To construct and analyze the model, we used the BioUML platform (https://sirius-web.org/bioumlweb/), an open-source Java-based integrated environment designed for systems biology [84,85]. It supports a wide range of systems biology standards and mathematical methods for the simulation, parameter estimation, and analysis of computational models, including tools for their visual representation.

2.7. Numerical solution of the model

To simulate the PBPK model, we used CVODE solver [86] ported to Java and adapted to the BioUML programming interface.

2.8. Parameter fitting

The problem of identifying the model parameters is formulated by minimizing the objective function, which is defined as the sum of the normalized squared differences between the experimental (X_i^{exp}) and simulated (X_i) values of the model variables at time points t_j:

$$f_{dist}(X_1, \ldots, X_n) = \sum_{i=1}^{n} \sum_{j=1}^{m} \frac{\omega_{min}}{\omega_i} \left(X_i(t_j) - X_i^{exp}(t_j)\right)^2. \quad (8)$$

Weights are considered such that all variables (regardless of the order of magnitude) have the same importance in the fit:

$$\omega_i = \left| \frac{\sum_j X_i^{exp}(t_j)}{m} \right|, \omega_{min} = min\ \omega_i, i = 1, \ldots, n, j = 1, \ldots, m.$$

In the present study, we not only fitted the experimental time series with simulated curves, but also considered the additional parametric constraints imposed on the optimized permeability coefficients (*PAC*) of the lungs, liver, spleen, and kidneys. We assumed that these coefficients would increase over time after LPS administration. Because we used four experimental datasets of the temporal biodistribution of nanoparticles in the control group of mice (exp_1), as well as in the LPS-treated animals after 30 min (exp_2), 6 h (exp_3), and 24 h (exp_4), the corresponding constraints for each organ were defined as follows:

$$PAC_{exp_l} < PAC_{exp_{l+1}}, l = 1, \ldots, 3.$$

This caused the calculation of the penalty function for $s \in \{lungs, liver, spleen, kidneys\}$:

$$f_{penalty}(p_1, q_1, \ldots, p_s, q_s) = \sum_{l,s} \max\left(0, \left(PAC^s_{exp_l} - PAC^s_{exp_{l+1}}\right)\right)^2.$$

To solve the optimization problem described above, we used a stochastic ranking evolution strategy [87] suitable for constrained global optimization.

2.9. Identifiability analysis

Having a model that adequately describes the measured data, it is important to understand how accurately the parameters are determined in terms of the quantity and quality of the data. Such knowledge is necessary for further investigation of model predictions. Therefore, we tested the parameters of the proposed model for its identifiability. To do this, we used numerical analysis to explore the sensitivity of objective function (8) to the value changes in the fitting parameters. This methodology was described in detail by Raue et al. [88] Briefly, we excluded from the optimization process a single parameter with a fixed value, which gradually increased and then decreased depending on the initial solution. So, we determined the effect of this parameter on the value of the objective function (i.e., the quality of the experimental data approximation). If the shift of the considered parameter in any direction along the numeric axis leads to a significant increase in the objective function, then it is identifiable. Otherwise, it is not possible to determine the parameter based on available experimental data. In the current study, this analysis was used to test the fitted values of the *PAC* and *P* parameters used in Equations (3) and (4).

2.10. Statistical analysis

All the data are the result of a minimum of three independent experiments. Statistical analyses were performed using Prism GraphPad software. One-way ANOVA was employed to assess for significant differences between groups, followed by Dunnett's test for multiple comparisons with the control group. Statistical significance is denoted by asterisks: *P < 0.05, **P < 0.01, ***P < 0.001.

3. Results and discussion

3.1. Particle synthesis, characterization and toxicity in vitro

ANP was synthesized via desolvation/crosslinking, as shown by Kolesova et al. [73] DLS analysis showed an average diameter of 120 nm and a negative surface charge of −30 mV (Fig. 2a–c). Atomic force microscopy (AFM) and electron microscopy (STEM) analyses demonstrated a spherical regular shape and confirmed the high polydispersity of the carriers (Fig. 2d–e). ANP toxicity was tested on THP-1 human macrophage cell line differentiated into inflammatory cells, as described in the Materials and Methods section. The particles were administered at a relatively high concentration to the cells for 6 h, after which the culture medium was removed, the cells were washed, and the medium was replaced. Cell viability was measured after 72 h of incubation, demonstrating that all concentrations slightly decreased the cell viability in a non-significant manner.

3.2. In vivo ALI induction and particle treatment

Non-lethal ALI was induced in male BALB/c mice by intraperitoneal (i. p.) injection of LPS, as described in 2.4. At different time points after LPS administration (0.5, 6, and 24 h), the mice were intravenously injected with fluorescently labeled ANP, and their distribution in the lungs, liver, spleen, and kidneys was followed *ex-vivo* over a time window of 48 h. Representative images of the obtained results and overall data are shown in Fig. 3.

3.3. Model calibration

The model was adapted to four experimental datasets representing the temporal biodistribution of intravenously administered ANP in the control group of mice as well as in the treated animals 30 min, 6 h, and 24 h after intraperitoneal LPS injection.

Using the evolution strategy method described in the parameter-fitting section, we calibrated:

- *PAC* and *P* coefficients in Equations (3) and (4);
- coefficients *KRES*50, *KRESmax*, *KRESn*, and *KRESrelease* in Equations (5) and (6) that simulate the endocytic uptake and exocytic release of the administered ANP;
- coefficients *KurineC* and *KbileC* in Equation (7) that describe the excretion of ANP the urine and bile, respectively;
- unknown parameter *k*, which converts simulated nanoparticle concentrations into experimentally measured values of total radiant efficiency per luminous area.

According to the experimental protocol, we considered the following values for the average body weight (*BW*) and the administered dose of ANP (*PDOSEiv*):

$$BW = 0.024 \text{ kg}, PDOSEiv = 208 \text{ mg/kg (or 5 mg / 0.024 kg)}.$$

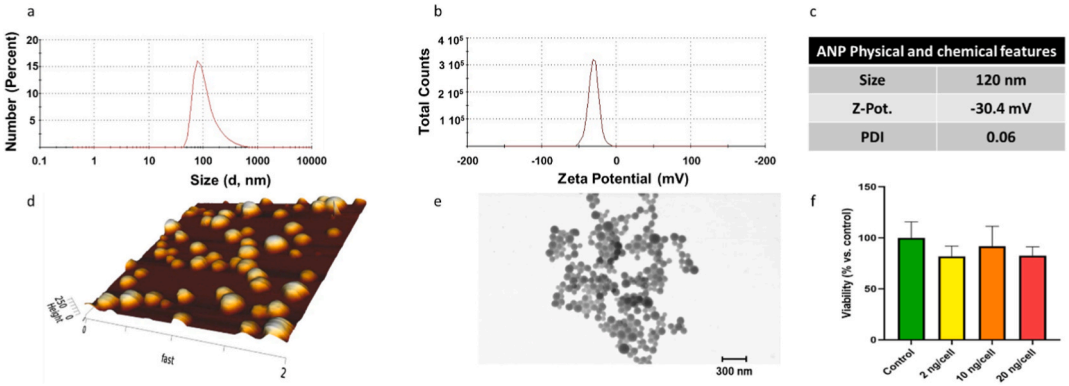

Fig. 2. Physical and chemical properties of the particles: (a) size and (b) surface charge analysis ANP; (c) summary table of the physical characteristics of the particles; investigation of particle size and shape via (d) AFM and (e) STEM analysis. (f) THP-1 macrophage viability upon treatment with increasing concentrations of ANP.

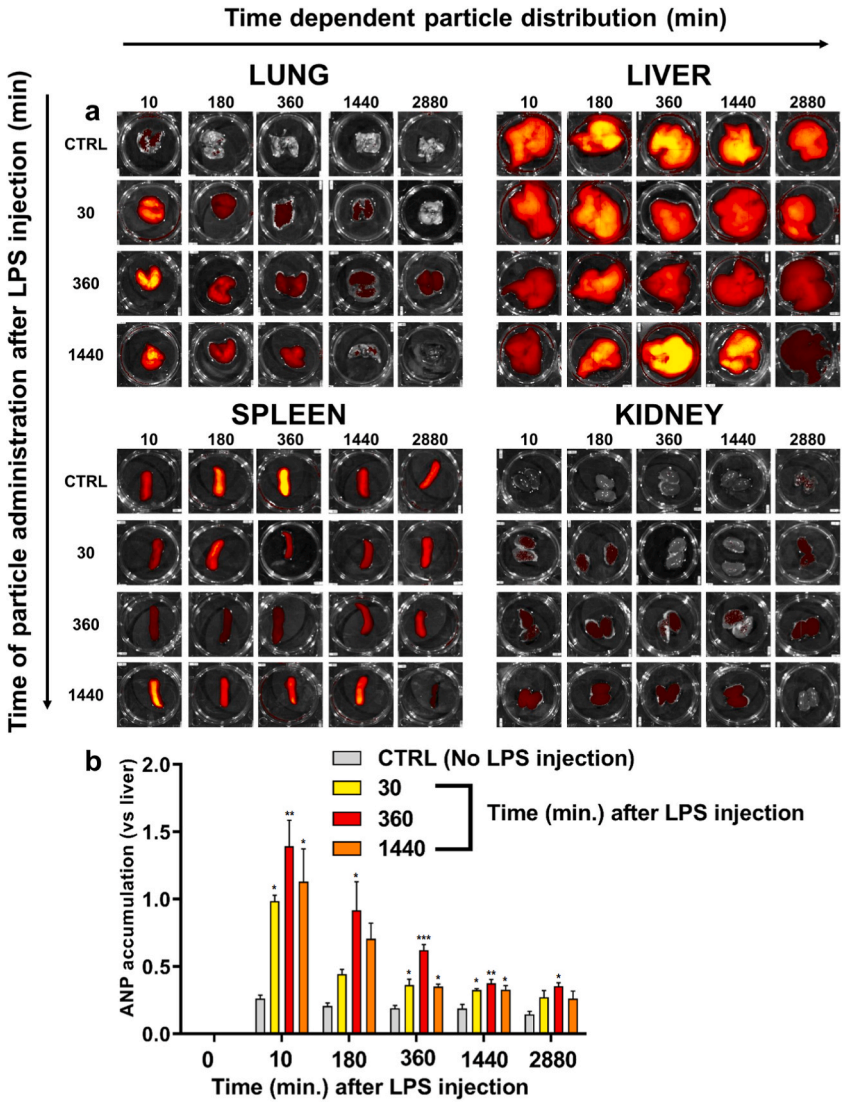

Fig. 3. *Ex vivo* IVIS analysis of lungs, liver, spleen and kidneys: (**a**) Representative pictures of the explanted organs were organized as a function of the time of particle administration after LPS injection and particle biodistribution kinetics. The fluorescent signal was measured and normalized against organ area. The obtained data were used to inform our computational model. (**b**) ANP pulmonary accumulation at different time points after LPS administration. Data were normalized against hepatic particle accumulation. $^{*}P < 0.05$, $^{**}P < 0.01$, $^{***}P < 0.001$ (*vs.* CTRL).

The remaining parameters (fractional blood flow rates, compartment volumes, and compartment capillary blood volumes) were taken from the model by Cheng et al. [69].

Parameter fitting was based on the following assumptions: the permeability (*PAC*) coefficients of the lungs, liver, spleen, and kidneys increased from the first (control) to the fourth (24 h after LPS injection) experiment; the distribution (*P*) coefficients of organ compartments are unique for each experiment; all other parameters have the same values in all experiments.

The model simulation results showed a good approximation of the experimental data for the biodistribution of ANP in mice following LPS administration. This was true for both the case of exact values of the total radiant efficiency per organ area (Supplementary Fig. 1) and the case of data calculated relative to hepatic ANP accumulation (Fig. 4). Tables 1 and 2 summarize the estimated values of the individual and common parameters, respectively.

3.4. Parameter identifiability

To analyze the changes in tissue permeability and ANP accumulation after LPS administration, we examined *PAC* and *P* parameters (Table 1), respectively, for their identifiability. The results of the distribution coefficient analysis are shown in Fig. 5, while the results obtained for the permeability coefficients are shown in Supplementary Fig. 2.

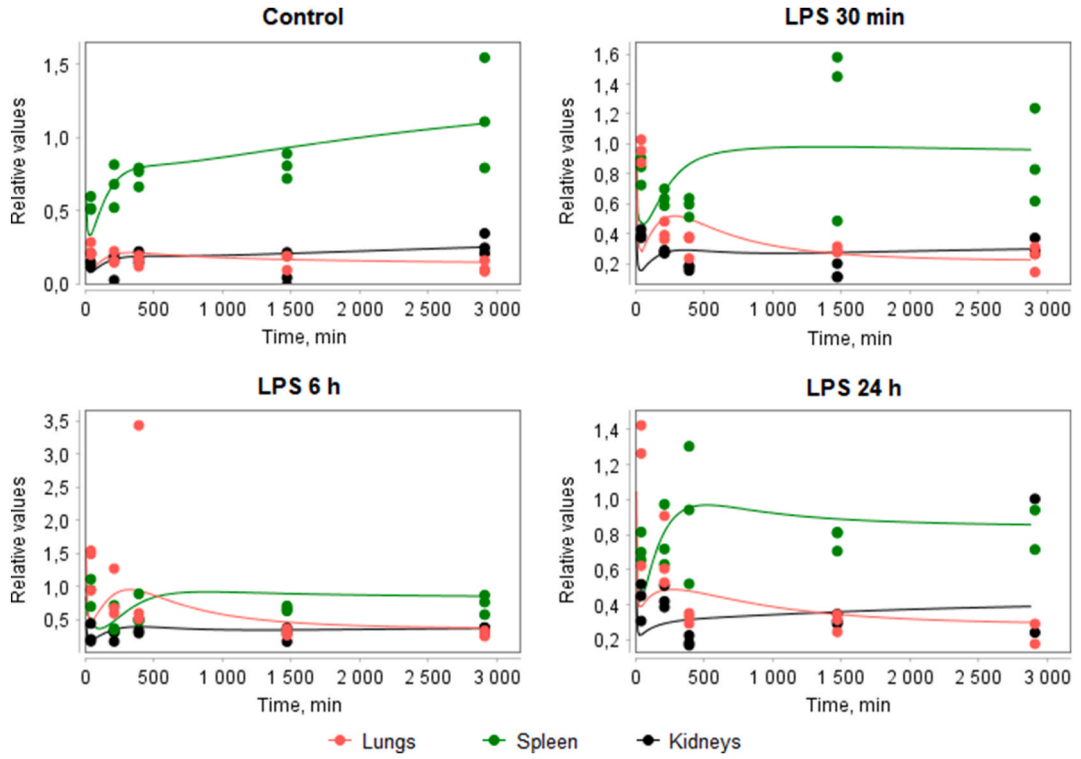

Fig. 4. Comparison of the PBPK model simulation results (solid lines) with the experimental distribution of ANP (dots) in lungs, spleen, and kidneys relative to the liver at difference time points after LPS injection.

Table 1
Fitting parameters of the PBPK model, which are different for the experiments.

Compartments	Control	LPS 30 min	LPS 6 h	LPS 24 h
P, distribution coefficients, unitless				
Lungs	0.32912	0.53913	0.89661	0.68027
Liver	0.33850	0.15396	0.18851	0.12654
Spleen	0.77655	0.54406	0.48332	0.49543
Kidneys	0.26674	0.18484	0.22915	0.23102
Rest of body	1.27424	1.63449	2.61706	8.19636
PAC, permeability coefficients, unitless				
Lungs	0.00010	0.00400	0.00444	0.04834
Liver	0.00082	0.00083	0.00090	0.00099
Spleen	0.03112	0.13851	0.31223	0.58405
Kidneys	0.00178	0.03171	0.03176	0.06059
Rest of body	0.65139	0.17960	1.29770	0.00246

Table 2
Fitting parameters of the PBPK model common for all experiments.

Parameters	Lungs	Liver	Spleen	Kidneys	Rest of body	Units
*KRES*50	12.5763	162.343	138.387	345.945	53.6192	min
KRESmax	0.09782	4.17318	20.8142	0.77376	0.81059	1/min
KRESn	1.69178	1.15243	1.97529	0.65725	25.4498	–
KRESrelease	0.00195	0.02254	0.09512	0.00302	0.16775	1/min
KurineC	–	–	–	2.7E-06	–	L/min
KbileC	–	3.4E-06	–	–	–	L/min
k	1358630.5					–

The following conclusions can be drawn based on the computational data. The value of *P*, which reflects ANP accumulation in the tissue, peaked in the lungs at 6 h after LPS treatment. Thus, the dynamics of this parameter reflected the experimental observations in the current study. The change in the accumulation of ANP in the lungs was measured after intravenous administration of nanoparticles.

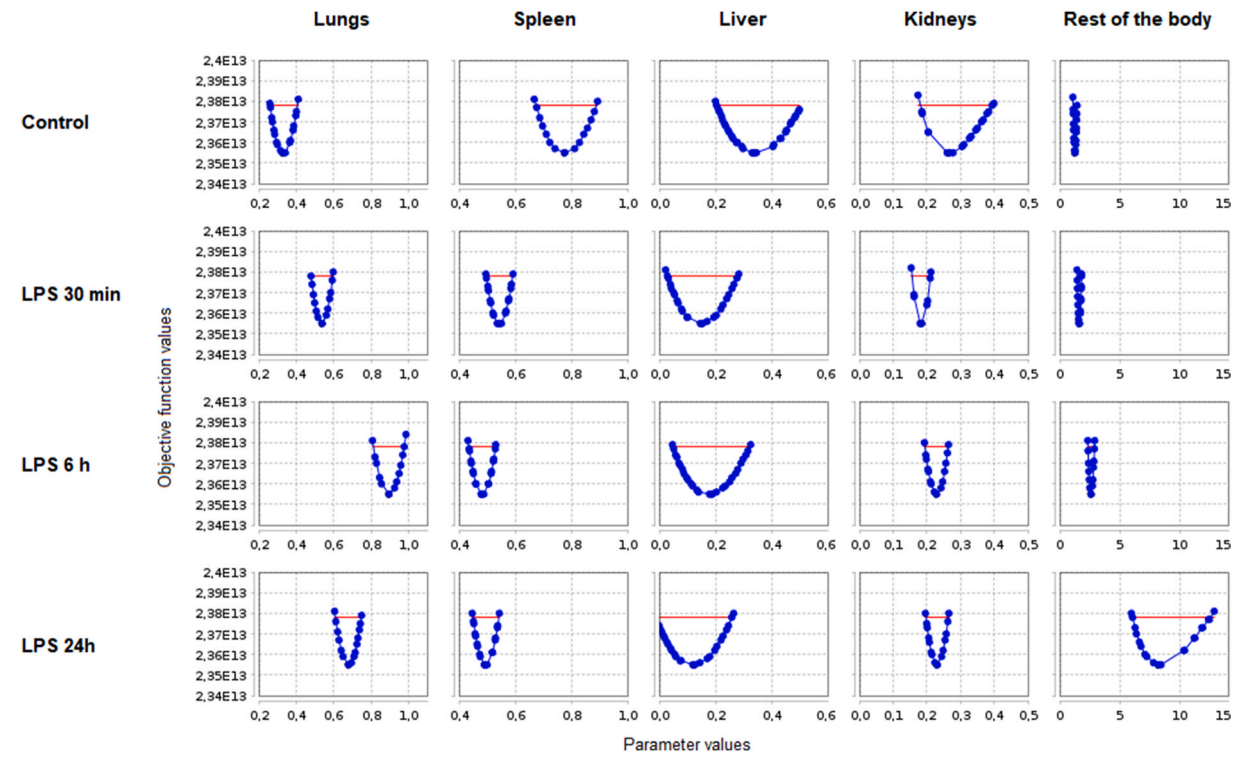

Fig. 5. Results of the identifiability analysis of distribution coefficients in the model (*P*, unitless). Parabolic functions mean that an increase or decrease in the parameter value found during optimization (the vertex of the parabola) leads to an increase in the objective function value, i.e., to deterioration of the quality of experimental data approximation. The red line indicates the 1%-threshold for increasing the objective function, which is considered as a condition for terminating the analysis.

Interestingly, Li et al. [89] obtained a similar trend (with a peak at 4 h after intratracheal instillation of LPS) in the accumulation of intratracheally administered ^{125}I-labeled bovine serum albumin in the blood of rats (i.e., for the reverse process of lung-to-blood permeability). Zhao et al. [90] received an estimate similar to that obtained in our study. In their experiments, LPS-induced microvascular injury in mice resulted in a maximum increase in the basal lung capillary filtration coefficient (reflecting fluid accumulation in the lungs owing to extravasation) at 6 h. In addition, several studies have revealed that LPS induces an increase in intravenously administered Evans blue dye in mouse lung tissue, but the dependence of the accumulated concentration on time after LPS administration was not analyzed [82,83,91].

The values of *P* in the LPS experiments in the liver, spleen, and kidneys were lower than those in the control experiment. This suggests that the accumulation of nanoparticles in these organs decreases after LPS injection, possibly because of an increase in the level of nanoparticles in the lungs and/or the rest of the body. In addition, an increase in *P*, with a sharp drop in *PAC* in the remaining tissues 24 h after LPS administration, led to a decrease in the *PAC*/*P* ratio, which acts as a kinetic constant in Equation (4). From the point of view of modeling, this is a consequence of the fact that ANP accumulation in the lung compartment is already declining by this time, whereas in the liver, spleen, and kidneys, it has not yet returned to the initial levels of the control experiment. This may indicate that 24 h after LPS administration, tissue repair is already underway in the lungs, while damage to the liver, spleen, and kidneys may persist. In the experiments by Verjans et al. [39] LPS caused lung mechanics in mice to deteriorate within the first 4 days and recover to day 10. However, this study used the intratracheal route of LPS administration and other mouse lineages (wild-type C57BL/6J and lymphocyte-deficient RAG2−/− mice).

Note that LPS injection induced a sharp increase (by one or two orders of magnitude) in the permeability parameters of the lungs and kidneys. Apparently, the values of these parameters reached the saturation thresholds in the model because their uncontrolled increase in the LPS experiments did not lead to a significant deterioration in the approximation of the experimental data. This result is consistent with experiments in which LPS stimulated an increase in pulmonary cell permeability, as assessed by a decrease in transepithelial/transendothelial electrical resistance [80,81]. Furthermore, splenic permeability coefficient increased over time after LPS administration. This indicated the progression of inflammation within 24 h of damage.

Eventually, the amount of experimental data is insufficient to draw any conclusions regarding liver permeability as a function of time after LPS injection. This is likely because the liver is the final destination of the particles. In all four experiments, the *PAC* parameters were partially identifiable, with comparable lower limits of the values.

Based on these results, it can be concluded that the therapeutic efficacy and distribution of nanocarriers in LPS-induced ALI in mice depends not only on the route of administration [55], but also on the time of administration after LPS injury.

3.5. Limitations of the study

- In the model, we did not consider the change in body weight of mice, although LPS can cause its decrease [92].
- We also did not consider the intracellular degradation of albumin in lysosomes [93–95], which is the most common final destination of internalized biological nanoparticles [73].

4. Conclusions

Computational modeling has become an increasingly important tool in experimental medicine. Specifically, it has been applied in the study of nanoparticle organ distribution in tumor diseases. However, other conditions, such as acute lung injury, have not been extensively investigated with this tool. Acute lung injury (ALI) is a life-threatening condition that can arise from several causes including infection, trauma, or exposure to toxic substances. Computational modeling can help researchers to understand the complex dynamics that occur in the lungs during such events. In this study, we simulated the kinetics of ANP pulmonary accumulation at different time points after LPS administration. The modular model developed in the BioUML platform allowed the simulation of the behavior of nanoparticles after pulmonary administration, characterized by further accumulation in the liver and spleen (to a minor extent in the kidneys), which was significantly delayed by inflammatory insults. The model showed that the distribution of nanoparticles in the organs depended on the time after LPS administration. Thus, the level of ANP in the lungs increased, reaching a peak 6 h after LPS damage, whereas the concentration of ANP in the liver, kidneys, and spleen decreased. The model predicts that LPS induces an immediate (within the first 30 min) dramatic increase in lung and kidney tissue permeability, whereas splenic tissue permeability gradually increases 24 h after LPS injection. These data confirm the role of inflammation in unbalanced mass transport within different organs and tissues, and this phenomenon is particularly relevant in the generation of computational models of nanoparticle biodistribution [96,97]. This information can then be used to inform the development of new therapies that can target specific organs affected by bacterial infections, thereby contributing to improved patient outcomes. Overall, the importance of computational modeling in this area of research cannot be overstated, as it promises to provide valuable insights into the mechanisms underlying this condition and helps develop effective therapies.

Ethic statement

This study was reviewed and approved by the N.N. Blokhin Medical Research Center of Oncology, ethical committee (Protocol Number 08P-13.12.2022). Our ethical approval adheres to ARRIVE guidelines.

Funding

This research was funded by the Russian Science Foundation (grant no. 21-75-30020). V.S.P. was supported by State Program of the Ministry of Science and Higher Education of the Russian Federation (no. 075-01551-23-00; FSSF-2023-0006).

Data availability

The implementation of the model is available in the web version of the BioUML platform and is stored in the GitLab repository at: https://gitlab.sirius-web.org/nanoparticles/models/-/tree/master/PBPK%20model%20for%20albumin%20NPs%20after%20LPS.

CRediT authorship contribution statement

Elena O. Kutumova: Formal analysis. **Ilya R. Akberdin:** Methodology. **Vera S. Egorova:** Investigation. **Ekaterina P. Kolesova:** Investigation. **Alessandro Parodi:** Supervision, Funding acquisition. **Vadim S. Pokrovsky:** Investigation. **Andrey A. Zamyatnin, Jr:** Funding acquisition. **Fedor A. Kolpakov:** Supervision.

Declaration of competing interest

The authors declare the following financial interests/personal relationships which may be considered as potential competing interests:E.O.K., I.R.A., and F.A.K. work for Biosoft.Ru, Ltd. The other authors declare no conflict of interest.

Appendix A

In this section we provide a mathematical formulation of the model.

A1. Common kinetic laws

r1. The rate of ANP entry into the capillary blood of the compartment:

$$v_1 = Q \cdot \frac{inputA}{inputV}, Q = QC \bullet QCC \bullet BW^{0.75},$$

where *inputV* is the input plasma volume, $QCC = 0.275$ L/min denotes the cardiac output in mice, *QC* determines the fraction of *QCC* specific to the compartment, and *BW* is body weight.

r2in. Diffusion of ANP through the capillary wall into the tissue interstitium depending on the permeability coefficient *PAC* and capillary blood volume *Vb*:

$$v_2^{in} = PAC \cdot Q \cdot \frac{Ab}{Vb}, Vb = V \cdot BV, V = BW \cdot VC.$$

where, *BV* is a fraction of the compartment volume *V*, and *VC* is a fraction of the body weight.

r2out. The reverse process with distribution coefficient *P* and tissue interstitium volume *Vt*:

$$v_2^{out} = \frac{PAC \cdot Q \cdot At}{Vt \cdot P}, Vt = V - Vb.$$

r3in. The rate of endocytic/phagocytic uptake of ANP, described by the Hill function with parameters *KRESmax* (maximum uptake rate), *KRES*50 (time to reach a half-maximum uptake rate), and *KRESn* (Hill coefficient):

$$v_3^{in} = KRESUP \cdot At, KRESUP = \frac{KRESmax \bullet t^{KRESn}}{KRES50^{KRESn} + t^{KRESn}}.$$

r3out. The rate of ANP release from endocytic/phagocytic cells, determined using the constant coefficient *KRESrelease*:

$$v_3^{out} = KRESrelease \cdot ARES.$$

r4. Outflow of ANP from capillary blood into the output plasma:

$$v_4 = Q \cdot \frac{Ab}{Vb}.$$

A2. Common equations

$$\frac{dAb}{dt} = v_1 - v_2^{in} + v_2^{out} - v_4, \frac{dAt}{dt} = v_2^{in} - v_2^{out} - v_3^{in} + v_3^{out}, \frac{dARES}{dt} = v_3^{in} - v_3^{out},$$

$$Atotal = Ab + At + ARES, Ctotal = \frac{Atotal}{V},$$

$$Atissue = At + ARES, Ctissue = \frac{Atissue}{Vt}.$$

A3. Lung module

Common equations with the specific constants:

$$QC = QLuC, BV = BVLu, VC = VLuC, PAC = PALuC, P = PLu,$$

$$KRES50 = KLuRES50, KRESmax = KLuRESmax,$$

$$KRESn = KLuRESn, KRESrelease = KLuRESrelease.$$

A4. Spleen module

Common equations with the specific constants:

$$QC = QSC, BV = BVS, VC = VSC, PAC = PASC, P = PS, KRES50 = KSRES50,$$

$$KRESmax = KSRESmax, KRESn = KSRESn, KRESrelease = KSRESrelease.$$

A5. Liver module

$$\frac{dALb}{dt} = v_1 - v_2^{in} + v_2^{out} - v_3^{in} + v_3^{out} - v_4, \frac{dALt}{dt} = v_2^{in} - v_2^{out} - v_b,$$

$$\frac{dALRES}{dt} = v_3^{in} - v_3^{out},$$

$$ALiver = ALb + ALt + ALRES, ALivert = ALt + ALRES,$$

$$CLiver = \frac{ALiver}{VL}, CLivert = \frac{ALivert}{VLt}.$$

The equations include the specific constants:

$$QC = QLC, BV = BVL, VC = VLC, PAC = PALC, P = PL, KRES50 = KLRES50,$$

$$KRESmax = KLRESmax, KRESn = KLRESn, KRESrelease = KLRESrelease.$$

VL and *VLt* denote the liver volume and liver tissue interstitial volume, respectively, whereas v_b is the rate of ANP excretion with bile (reaction *r*5 in Fig. 1c):

$$v_b = KbileC \cdot BW^{0.75} \cdot \frac{ALt}{VLt}.$$

Here, *ALt* is the amount of ANP in the liver tissue, *VLt* is the liver tissue volume, and *KbileC* is a constant.

A6. Kidney module

In addition to the common equations with the specific constants:

$$QC = QKC, BV = BVK, VC = VKC, PAC = PAKC, P = PK, KRES50 = KKRES50,$$

$$KRESmax = KKRESmax, KRESn = KKRESn, KRESrelease = KKRESrelease,$$

the kidney compartment includes the reaction of ANP excretion from capillary blood through the urinary tract, which proceeds at the following rate:

$$v_u = KurineC \cdot BW^{0.75} \cdot \frac{AKb}{VKb},$$

where *VKb* and *AKb* denote the parameters originating from the common structure module and determining the volume of capillary blood of the kidneys and the amount of ANP in this volume, respectively, and *KurineC* is a constant.

A7. The rest of the body module

Common equations with the specific constants:

$$BV = BVR, PAC = PARC, P = PR, KRES50 = KRRES50,$$

$$KRESmax = KRRESmax, KRESn = KRRESn, KRESrelease = KRRESrelease.$$

A8. Venous plasma module

The rate of intravenous administration of ANP is calculated using injection time (*Timeiv*), injected dose (*PDOSEiv*), and body weight (*BW*) as follows:

$$\frac{dAV}{dt} = RIV = \begin{cases} \frac{PDOSEiv \bullet BW}{Timeiv}, & \text{if } t < Timeiv, \\ 0, & \text{otherwise,} \end{cases}$$

where *AV* is the amount of ANP in venous plasma. The compartment volume *VPv* is assumed to be 80 % of the total plasma volume, which is calculated as a fraction *VPIC* of *BW*:

$$VPv = BW \bullet VPlC \bullet 0.8.$$

The venous concentration of ANP is defined by the ratio:

$$CV = \frac{AV}{VPv}.$$

A9. Arterial plasma module

The arterial plasma volume *APv* is 20 % of the total plasma volume, which is equivalent to 25 % of *VPv*:

$$APv = 0.25 \bullet VPv.$$

The arterial concentration of ANP (*CA*) is equal to the amount (*AA*) divided by the *APv*:

$$CA = \frac{AA}{APv}.$$

A10. The top level of the model

The top diagram level includes algebraic equations to calculate volume of the rest of the body *VRC* from the fractional volumes of plasma (*VPlC*), lungs (*VLuC*), spleen (*VSC*), liver (*VLC*), and kidneys (*VKC*):

$$VRC = 1 - (VLC + VSC + VKC + VLuC + VPlC),$$

and to find blood flow to the rest of the body *QRC* from the fractional blood flows to liver (*QLC*), spleen (*QSC*), and kidneys (*QKC*):

$$QRC = 1 - (QLC + QSC + QKC).$$

The equations that convert simulated ANP concentrations in the tissues of the lungs (*CLuT* or *CTissue* in terms of the common structure module), spleen (*CST*), kidneys (*CKT*), and liver ($CLT = CLiverT$) to the experimentally measured values of the average total radiant efficiency of organs (*TRELu*, *TRES*, *TREK*, and *TREL*, respectively) are defined as follows:

$$TRELu = k \bullet CLuT, TRES = k \bullet CST, TREK = k \bullet CKT, TREL = k \bullet CLT,$$

where *k* is a fitted constant.

Appendix A. Supplementary data

Supplementary data to this article can be found online at https://doi.org/10.1016/j.heliyon.2024.e30962.

References

[1] K. Tsushima, L.S. King, N.R. Aggarwal, A. De Gorordo, F.R. D'Alessio, K. Kubo, Acute lung injury review, Intern. Med. 48 (2009) 621–630, https://doi.org/10.2169/internalmedicine.48.1741.

[2] E.R. Johnson, M.A. Matthay, Acute lung injury: epidemiology, pathogenesis, and treatment, J. Aerosol Med. Pulm. Drug Deliv. 23 (2010) 243–252, https://doi.org/10.1089/jamp.2009.0775.

[3] H. Laycock, A. Rajah, Acute lung injury and acute respiratory distress syndrome: a review article, Br. J. Med. Pract. 3 (2) (2010) 324.

[4] V. Fanelli, V.M. Ranieri, Mechanisms and clinical consequences of acute lung injury, Ann Am Thorac Soc 12 (Suppl 1) (2015) S3–S8, https://doi.org/10.1513/AnnalsATS.201407-340MG.

[5] M.A. Matthay, R.L. Zemans, G.A. Zimmerman, Y.M. Arabi, J.R. Beitler, A. Mercat, M. Herridge, A.G. Randolph, C.S. Calfee, Acute respiratory distress syndrome, Nat. Rev. Dis. Prim. 5 (2019) 18, https://doi.org/10.1038/s41572-019-0069-0.

[6] B.M. Varisco, The pharmacology of acute lung injury in sepsis, Adv Pharmacol Sci. 2011 (2011) 1–7, https://doi.org/10.1155/2011/254619.

[7] J.A. Englert, C. Bobba, R.M. Baron, Integrating molecular pathogenesis and clinical translation in sepsis-induced acute respiratory distress syndrome, JCI Insight 4 (2019) e124061, https://doi.org/10.1172/jci.insight.124061.

[8] Q. Hu, C. Hao, S. Tang, From sepsis to acute respiratory distress syndrome (ARDS): emerging preventive strategies based on molecular and genetic researches, Biosci. Rep. 40 (2020) BSR20200830, https://doi.org/10.1042/BSR20200830.

[9] H. Gong, Y. Chen, M. Chen, J. Li, H. Zhang, S. Yan, C. Lv, Advanced development and mechanism of sepsis-related acute respiratory distress syndrome, Front. Med. 9 (2022) 1043859, https://doi.org/10.3389/fmed.2022.1043859.

[10] T.T. Bauer, S. Ewig, A.C. Rodloff, E.E. Muller, Acute respiratory distress syndrome and pneumonia: a comprehensive review of clinical data, Clin. Infect. Dis. 43 (2006) 748–756, https://doi.org/10.1086/506430.

[11] M.E. Long, R.K. Mallampalli, J.C. Horowitz, Pathogenesis of pneumonia and acute lung injury, Clin. Sci. (Lond.) 136 (2022) 747–769, https://doi.org/10.1042/CS20210879.

[12] R.D. Fremont, T. Koyama, C.S. Calfee, W. Wu, L.A. Dossett, F.R. Bossert, D. Mitchell, N. Wickersham, G.R. Bernard, M.A. Matthay, et al., Acute lung injury in patients with traumatic injuries: utility of a panel of biomarkers for diagnosis and pathogenesis, J. Trauma 68 (2010) 1121–1127, https://doi.org/10.1097/TA.0b013e3181c40728.

[13] M. Bakowitz, B. Bruns, M. McCunn, Acute lung injury and the acute respiratory distress syndrome in the injured patient, Scand. J. Trauma Resuscitation Emerg. Med. 20 (2012) 54, https://doi.org/10.1186/1757-7241-20-54.

[14] A. Tran, S.M. Fernando, L.J. Brochard, E. Fan, K. Inaba, N.D. Ferguson, C.S. Calfee, K.E.A. Burns, D. Brodie, V.A. McCredie, et al., Prognostic factors for development of acute respiratory distress syndrome following traumatic injury: a systematic review and meta-analysis, Eur. Respir. J. 59 (2022) 2100857, https://doi.org/10.1183/13993003.00857-2021.

[15] J.L. Larson, H.T. Robertson, S.F. Grey, S.A. Schobel, B.K. Potter, E.A. Elster, Acute respiratory distress syndrome and acute lung injury in a trauma population with and without long bone fractures, Front Syst Biol 2 (2023) 1058603, https://doi.org/10.3389/fsysb.2022.1058603.

[16] S. Taran, D.M. Hamad, S. Von Düring, A.K. Malhotra, A.A. Veroniki, V.A. McCredie, J.M. Singh, B. Hansen, M. Englesakis, N.K.J. Adhikari, Factors associated with acute respiratory distress syndrome in brain-injured patients: a systematic review and meta-analysis, J. Crit. Care 77 (2023) 154341, https://doi.org/10.1016/j.jcrc.2023.154341.

[17] K. Raghavendran, J. Nemzek, L.M. Napolitano, P.R. Knight, Aspiration-induced lung injury, Crit. Care Med. 39 (2011) 818–826, https://doi.org/10.1097/CCM.0b013e31820a856b.

[18] L.A. Mandell, M.S. Niederman, Aspiration pneumonia, N. Engl. J. Med. 380 (2019) 651–663, https://doi.org/10.1056/NEJMra1714562.

[19] P. Košutová, P. Mikolka, Aspiration syndromes and associated lung injury: incidence, pathophysiology and management, Physiol. Res. (2021) S567–S583, https://doi.org/10.33549/physiolres.934767.

[20] E.M. Summerhill, G.W. Hoyle, S.-E. Jordt, B.J. Jugg, J.G. Martin, S. Matalon, S.E. Patterson, D.J. Prezant, A.M. Sciuto, E.R. Svendsen, et al., An official American Thoracic Society workshop report: chemical inhalational disasters. Biology of lung injury, development of novel therapeutics, and medical preparedness, Ann Am Thorac Soc 14 (2017) 1060–1072, https://doi.org/10.1513/AnnalsATS.201704-297WS.

[21] C.T. Cowl, Assessment and treatment of acute toxic inhalations, Curr. Opin. Pulm. Med. 25 (2019) 211–216, https://doi.org/10.1097/MCP.0000000000000560.

[22] B. Guo, Y. Bai, Y. Ma, C. Liu, S. Wang, R. Zhao, J. Dong, H.-L. Ji, Preclinical and clinical studies of smoke-inhalation-induced acute lung injury: update on both pathogenesis and innovative therapy, Ther. Adv. Respir. Dis. 13 (2019) 175346661984790, https://doi.org/10.1177/1753466619847901.

[23] C. Cao, L. Zhang, J. Shen, Phosgene-induced acute lung injury: approaches for mechanism-based treatment strategies, Front. Immunol. 13 (2022) 917395, https://doi.org/10.3389/fimmu.2022.917395.

[24] A. Stoll, D.P. Shenton, A.C. Green, J.L. Holley, Comparative aspects of ricin toxicity by inhalation, Toxins 15 (2023) 281, https://doi.org/10.3390/toxins15040281.

[25] S.E. Rossi, J.J. Erasmus, H.P. McAdams, T.A. Sporn, P.C. Goodman, Pulmonary drug toxicity: radiologic and pathologic manifestations, Radiographics 20 (2000) 1245–1259, https://doi.org/10.1148/radiographics.20.5.g00se081245.

[26] M. Nishino, H. Hatabu, L.M. Sholl, N.H. Ramaiya, Thoracic complications of precision cancer therapies: a practical guide for radiologists in the new era of cancer care, Radiographics 37 (2017) 1371–1387, https://doi.org/10.1148/rg.2017170015.

[27] C.J. Shields, D.C. Winter, H.P. Redmond, Lung injury in acute pancreatitis: mechanisms, prevention, and therapy, Curr. Opin. Crit. Care 8 (2002) 158–163, https://doi.org/10.1097/00075198-200204000-00012.

[28] H. Akbarshahi, A.H. Rosendahl, G. Westergren-Thorsson, R. Andersson, Acute lung injury in acute pancreatitis – awaiting the big leap, Respir. Med. 106 (2012) 1199–1210, https://doi.org/10.1016/j.rmed.2012.06.003.

[29] M.-T. Zhou, Acute lung injury and ARDS in acute pancreatitis: mechanisms and potential intervention, World J. Gastroenterol. 16 (2010) 2094, https://doi.org/10.3748/wjg.v16.i17.2094.

[30] S.T. Tsikis, S.C. Fligor, T.I. Hirsch, A. Pan, L.J. Yu, H. Kishikawa, M.M. Joiner, P.D. Mitchell, M. Puder, Lipopolysaccharide-induced murine lung injury results in long-term pulmonary changes and downregulation of angiogenic pathways, Sci. Rep. 12 (2022) 10245, https://doi.org/10.1038/s41598-022-14618-8.

[31] D. Liu, M. Long, L. Gao, Y. Chen, F. Li, Y. Shi, N. Gu, Nanomedicines targeting respiratory injuries for pulmonary disease management, Adv. Funct. Mater. 32 (2022) 2112258, https://doi.org/10.1002/adfm.202112258.

[32] S. Bian, H. Cai, Y. Cui, W. Liu, C. Xiao, Nanomedicine-based therapeutics to combat acute lung injury, Int. J. Nanomed. 16 (2021) 2247–2269, https://doi.org/10.2147/IJN.S300594.

[33] P. Prasanna, S. Rathee, A. Upadhyay, S. Sulakshana, Nanotherapeutics in the treatment of acute respiratory distress syndrome, Life Sci. 276 (2021) 119428, https://doi.org/10.1016/j.lfs.2021.119428.

[34] Q. Qiao, X. Liu, T. Yang, K. Cui, L. Kong, C. Yang, Z. Zhang, Nanomedicine for acute respiratory distress syndrome: the latest application, targeting strategy, and rational design, Acta Pharm. Sin. B 11 (2021) 3060–3091, https://doi.org/10.1016/j.apsb.2021.04.023.

[35] A. Singh, S. Chakraborty, S.W. Wong, N.A. Hefner, A. Stuart, A.S. Qadir, A. Mukhopadhyay, K. Bachmaier, J.-W. Shin, J. Rehman, et al., Nanoparticle Targeting of de Novo Profibrotic Macrophages Mitigates Lung Fibrosis, Proc. Natl. Acad. Sci. U.S.A. 119 (2022) e2121098119, https://doi.org/10.1073/pnas.2121098119.

[36] G. Matute-Bello, C.W. Frevert, T.R. Martin, Animal models of acute lung injury, Am. J. Physiol. Lung Cell Mol. Physiol. 295 (2008) L379–L399, https://doi.org/10.1152/ajplung.00010.2008.

[37] D. Rittirsch, M.A. Flierl, D.E. Day, B.A. Nadeau, S.R. McGuire, L.M. Hoesel, K. Ipaktchi, F.S. Zetoune, J.V. Sarma, L. Leng, et al., Acute lung injury induced by lipopolysaccharide is independent of complement activation, J. Immunol. 180 (2008) 7664–7672, https://doi.org/10.4049/jimmunol.180.11.7664.

[38] T. Aoyagi, N. Yamamoto, M. Hatta, D. Tanno, A. Miyazato, K. Ishii, K. Suzuki, T. Nakayama, M. Taniguchi, H. Kunishima, et al., Activation of pulmonary invariant NKT cells leads to exacerbation of acute lung injury caused by LPS through local production of IFN- and TNF- by Gr-1+ Monocytes, Int. Immunol. 23 (2011) 97–108, https://doi.org/10.1093/intimm/dxq460.

[39] E. Verjans, S. Kanzler, K. Ohl, A.D. Rieg, N. Ruske, A. Schippers, N. Wagner, K. Tenbrock, S. Uhlig, C. Martin, Initiation of LPS-induced pulmonary dysfunction and its recovery occur independent of T cells, BMC Pulm. Med. 18 (2018) 174, https://doi.org/10.1186/s12890-018-0741-2.

[40] W. Lee, C.H. Lee, J. Lee, Y. Jeong, J.-H. Park, I.-J. Nam, D.S. Lee, H.M. Lee, J. Lee, N. Yun, et al., Botanical formulation, TADIOS, alleviates lipopolysaccharide (LPS)-Induced acute lung injury in mice via modulation of the Nrf2-HO-1 signaling pathway, J. Ethnopharmacol. 270 (2021) 113795, https://doi.org/10.1016/j.jep.2021.113795.

[41] D.-L. Hao, Y.-J. Wang, J.-Y. Yang, R. Xie, L.-Y. Jia, J.-T. Cheng, H. Ma, J.-X. Tian, S.-S. Guo, T. Liu, et al., The alleviation of LPS-induced murine acute lung injury by GSH-mediated PEGylated artesunate prodrugs, Front. Pharmacol. 13 (2022) 860492, https://doi.org/10.3389/fphar.2022.860492.

[42] R.S. Stephens, L. Johnston, L. Servinsky, B.S. Kim, M. Damarla, The tyrosine kinase inhibitor imatinib prevents lung injury and death after intravenous LPS in mice, Phys. Rep. 3 (2015) e12589, https://doi.org/10.14814/phy2.12589.

[43] L. Nie, W. Wu, Z. Lu, G. Zhu, J. Liu, CXCR3 may help regulate the inflammatory response in acute lung injury via a pathway modulated by IL-10 secreted by CD8 + CD122+ regulatory T cells, Inflammation 39 (2016) 526–533, https://doi.org/10.1007/s10753-015-0276-0.

[44] Q. Gong, L. He, M. Wang, S. Zuo, H. Gao, Y. Feng, L. Du, Y. Luo, J. Li, Comparison of the TLR4/NFκB and NLRP3 signalling pathways in major organs of the mouse after intravenous injection of lipopolysaccharide, Pharm. Biol. 57 (2019) 555–563, https://doi.org/10.1080/13880209.2019.1653326.

[45] Q. Li, L. Liu, H. Sun, K. Cao, Carnosic acid protects against lipopolysaccharide-induced acute lung injury in mice, Exp. Ther. Med. (2019), https://doi.org/10.3892/etm.2019.8042.

[46] Q. Wang, J. Wang, M. Hu, Y. Yang, L. Guo, J. Xu, C. Lei, Y. Jiao, J. Xu, Uncoupling protein 2 increases susceptibility to lipopolysaccharide-induced acute lung injury in mice, Mediat. Inflamm. 2016 (2016) 1–13, https://doi.org/10.1155/2016/9154230.

[47] S.A. Lee, S.H. Lee, J.Y. Kim, W.S. Lee, Effects of glycyrrhizin on lipopolysaccharide-induced acute lung injury in a mouse model, J. Thorac. Dis. 11 (2019) 1287–1302, https://doi.org/10.21037/jtd.2019.04.14.

[48] H. Li, Y. Hao, L. Yang, X. Wang, X. Li, S. Bhandari, J. Han, Y. Liu, Y. Gong, A. Scott, et al., MCTR1 alleviates lipopolysaccharide-induced acute lung injury by protecting lung endothelial glycocalyx, J. Cell. Physiol. 235 (2020) 7283–7294, https://doi.org/10.1002/jcp.29628.

[49] A.M. Abdelhamid, M. El Deeb, M.A. Zaafan, The protective effect of xanthenone against LPS-induced COVID-19 acute respiratory distress syndrome (ARDS) by modulating the ACE2/Ang-1-7 signaling pathway, Eur. Rev. Med. Pharmacol. Sci. 26 (2022) 5285–5296, https://doi.org/10.26355/eurrev_202207_29320.

[50] N. De Souza Xavier Costa, G. Ribeiro Júnior, A.A. Dos Santos Alemany, L. Belotti, D.H. Zati, M. Frota Cavalcante, M. Matera Veras, S. Ribeiro, E.G. Kallás, P. H. Nascimento Saldiva, et al., Early and late pulmonary effects of nebulized LPS in mice: an acute lung injury model, PLoS One 12 (2017) e0185474, https://doi.org/10.1371/journal.pone.0185474.

[51] S.B. Lim, I. Rubinstein, R.T. Sadikot, J.E. Artwohl, H. Önyüksel, A novel peptide nanomedicine against acute lung injury: GLP-1 in phospholipid micelles, Pharm. Res. (N. Y.) 28 (2011) 662–672, https://doi.org/10.1007/s11095-010-0322-4.

[52] S. Li, L. Chen, G. Wang, L. Xu, S. Hou, Z. Chen, X. Xu, X. Wang, F. Liu, Y.-Z. Du, Anti-ICAM-1 antibody-modified nanostructured lipid carriers: a pulmonary vascular endothelium-targeted device for acute lung injury therapy, J. Nanobiotechnol. 16 (2018) 105, https://doi.org/10.1186/s12951-018-0431-5.

[53] S.-J. Li, X.-J. Wang, J.-B. Hu, X.-Q. Kang, L. Chen, X.-L. Xu, X.-Y. Ying, S.-P. Jiang, Y.-Z. Du, Targeting delivery of simvastatin using ICAM-1 antibody-conjugated nanostructured lipid carriers for acute lung injury therapy, Drug Deliv. 24 (2017) 402–413, https://doi.org/10.1080/10717544.2016.1259369.

[54] P. Merckx, L. De Backer, L. Van Hoecke, R. Guagliardo, M. Echaide, P. Baatsen, B. Olmeda, X. Saelens, J. Pérez-Gil, S.C. De Smedt, et al., Surfactant protein B (SP-B) enhances the cellular siRNA delivery of proteolipid coated nanogels for inhalation therapy, Acta Biomater. 78 (2018) 236–246, https://doi.org/10.1016/j.actbio.2018.08.012.

[55] L. Wang, Y. Rao, X. Liu, L. Sun, J. Gong, H. Zhang, L. Shen, A. Bao, H. Yang, Administration route governs the therapeutic efficacy, biodistribution and macrophage targeting of anti-inflammatory nanoparticles in the lung, J. Nanobiotechnol. 19 (2021) 56, https://doi.org/10.1186/s12951-021-00803-w.

[56] J.W. Myerson, P.N. Patel, K.M. Rubey, M.E. Zamora, M.H. Zaleski, N. Habibi, L.R. Walsh, Y.-W. Lee, D.C. Luther, L.T. Ferguson, et al., Supramolecular arrangement of protein in nanoparticle structures predicts nanoparticle tropism for neutrophils in acute lung inflammation, Nat. Nanotechnol. 17 (2022) 86–97, https://doi.org/10.1038/s41565-021-00997-y.

[57] E.O. Kutumova, I.R. Akberdin, I.N. Kiselev, R.N. Sharipov, V.S. Egorova, A.O. Syrocheva, A. Parodi, A.A. Zamyatnin, F.A. Kolpakov, Physiologically based pharmacokinetic modeling of nanoparticle biodistribution: a review of existing models, simulation software, and data analysis tools, Int. J. Mol. Sci. 23 (2022) 12560, https://doi.org/10.3390/ijms232012560.

[58] M. Li, K.T. Al-Jamal, K. Kostarelos, J. Reineke, Physiologically based pharmacokinetic modeling of nanoparticles, ACS Nano 4 (2010) 6303–6317, https://doi.org/10.1021/nn1018818.

[59] D. Yuan, H. He, Y. Wu, J. Fan, Y. Cao, Physiologically based pharmacokinetic modeling of nanoparticles, J. Pharmaceut. Sci. 108 (2019) 58–72, https://doi.org/10.1016/j.xphs.2018.10.037.

[60] Y. Wenger, R.J. Schneider II, G.R. Reddy, R. Kopelman, O. Jolliet, M.A. Philbert, Tissue distribution and pharmacokinetics of stable polyacrylamide nanoparticles following intravenous injection in the rat, Toxicol. Appl. Pharmacol. 251 (2011) 181–190, https://doi.org/10.1016/j.taap.2010.11.017.

[61] G. Bachler, N. von Goetz, K. Hungerbühler, A physiologically based pharmacokinetic model for ionic silver and silver nanoparticles, Int. J. Nanomed. 8 (2013) 3365–3382, https://doi.org/10.2147/ijn.s46624.

[62] D. Li, G. Johanson, C. Emond, U. Carlander, M. Philbert, O. Jolliet, Physiologically based pharmacokinetic modeling of polyethylene glycol-coated polyacrylamide nanoparticles in rats, Nanotoxicology 8 (2014) 128–137, https://doi.org/10.3109/17435390.2013.863406.

[63] Z. Lin, N.A. Monteiro-Riviere, J.E. Riviere, A physiologically based pharmacokinetic model for polyethylene glycol-coated gold nanoparticles of different sizes in adult mice, Nanotoxicology 10 (2016) 162–172, https://doi.org/10.3109/17435390.2015.1027314.

[64] B.A. Howell, A. Chauhan, A physiologically based pharmacokinetic (PBPK) model for predicting the efficacy of drug overdose treatment with liposomes in man, J. Pharmaceut. Sci. 99 (2010) 3601–3619, https://doi.org/10.1002/jps.22115.

[65] L. Kagan, P. Gershkovich, K.M. Wasan, D.E. Mager, Dual physiologically based pharmacokinetic model of liposomal and nonliposomal amphotericin B disposition, Pharm. Res. (N. Y.) 31 (2014) 35–45, https://doi.org/10.1007/s11095-013-1127-z.

[66] X.-F. Lu, K. Bi, X. Chen, Physiologically based pharmacokinetic model of docetaxel and interspecies scaling: comparison of simple injection with folate receptor-targeting amphiphilic copolymer-modified liposomes, Xenobiotica 46 (2016) 1093–1104, https://doi.org/10.3109/00498254.2016.1155128.

[67] F. Kullenberg, O. Degerstedt, C. Calitz, N. Pavlović, D. Balgoma, J. Gråsjö, E. Sjögren, M. Hedeland, F. Heindryckx, H. Lennernäs, In vitro cell toxicity and intracellular uptake of doxorubicin exposed as a solution or liposomes: implications for treatment of hepatocellular carcinoma, Cells 10 (2021) 1717, https://doi.org/10.3390/cells10071717.

[68] S. Perazzolo, D.D. Shen, R.J. Ho, Physiologically based pharmacokinetic modeling of 3 HIV drugs in combination and the role of lymphatic system after subcutaneous dosing. Part 2: model for the drug-combination nanoparticles, J. Pharmaceut. Sci. 111 (2022) 825–837, https://doi.org/10.1016/j.xphs.2021.10.009.

[69] Y.-H. Cheng, C. He, J.E. Riviere, N.A. Monteiro-Riviere, Z. Lin, Meta-analysis of nanoparticle delivery to tumors using a physiologically based pharmacokinetic modeling and simulation approach, ACS Nano 14 (2020) 3075–3095, https://doi.org/10.1021/acsnano.9b08142.

[70] Z. Wang, J. Li, J. Cho, A.B. Malik, Prevention of vascular inflammation by nanoparticle targeting of adherent neutrophils, Nat. Nanotechnol. 9 (2014) 204–210, https://doi.org/10.1038/nnano.2014.17.

[71] A. Singh, S. Chakraborty, S.W. Wong, N.A. Hefner, A. Stuart, A.S. Qadir, A. Mukhopadhyay, K. Bachmaier, J.-W. Shin, J. Rehman, et al., Nanoparticle Targeting of de Novo Profibrotic Macrophages Mitigates Lung Fibrosis, Proc. Natl. Acad. Sci. U.S.A. 119 (2022) e2121098119, https://doi.org/10.1073/pnas.2121098119.

[72] K. Bachmaier, A. Stuart, A. Singh, A. Mukhopadhyay, S. Chakraborty, Z. Hong, L. Wang, Y. Tsukasaki, M. Maienschein-Cline, B.B. Ganesh, et al., Albumin nanoparticle endocytosing subset of neutrophils for precision therapeutic targeting of inflammatory tissue injury, ACS Nano 16 (2022) 4084–4101, https://doi.org/10.1021/acsnano.1c09762.

[73] E.P. Kolesova, V.S. Egorova, A.O. Syrocheva, A.S. Frolova, D. Kostyushev, A. Kostyusheva, S. Brezgin, D.B. Trushina, L. Fatkhutdinova, M. Zyuzin, et al., Proteolytic resistance determines albumin nanoparticle drug delivery properties and increases cathepsin B, D, and G expression, Int. J. Mol. Sci. 24 (2023) 10245, https://doi.org/10.3390/ijms241210245.

[74] J.O. Martinez, A. Parodi, X. Liu, M.G. Kolonin, M. Ferrari, E. Tasciotti, Evaluation of cell function upon nanovector internalization, Small 9 (9–10) (2013) 1696–1702, https://doi.org/10.1002/smll.201202001.

[75] T. Maehara, F. Higashitarumi, R. Kondo, K. Fujimori, Prostaglandin $F_{2\alpha}$ receptor antagonist attenuates LPS-induced systemic inflammatory response in mice, Faseb. J. 34 (11) (2020) 15197–15207, https://doi.org/10.1096/fj.202001481R.

[76] E. Kutumova, I. Akberdin, I. Kiselev, R. Sharipov, F. Kolpakov, Modular representation of physiologically based pharmacokinetic models: nanoparticle delivery to solid tumors in mice as an example, Mathematics 10 (2022) 1176, https://doi.org/10.3390/math10071176.

[77] J. Bourquin, D. Septiadi, D. Vanhecke, S. Balog, L. Steinmetz, M. Spuch-Calvar, P. Taladriz-Blanco, A. Petri-Fink, B. Rothen-Rutishauser, Reduction of nanoparticle load in cells by mitosis but not exocytosis, ACS Nano 13 (2019) 7759–7770, https://doi.org/10.1021/acsnano.9b01604.

[78] N. Oh, J.H. Park, Endocytosis and exocytosis of nanoparticles in mammalian cells, Int. J. Nanomed. 51 (2014), https://doi.org/10.2147/IJN.S26592.

[79] A. Parodi, M.V. Voronina, A.A. Zamyatnin, The importance of nanocarriers' intra- and extracellular degradation:what we know and should know about it? Curr. Med. Chem. 31 (2023) 128–132, https://doi.org/10.2174/0929867330666230315144546.

[80] Y. Xiang, S. Zhang, J. Lu, W. Zhang, M. Cai, D. Qiu, D. Cai, USP9X promotes LPS-induced pulmonary epithelial barrier breakdown and hyperpermeability by activating an NF-κBp65 feedback loop, Am. J. Physiol. Cell Physiol. 317 (2019) C534–C543, https://doi.org/10.1152/ajpcell.00094.2019.

[81] K.-T. Kubra, M.A. Uddin, N. Barabutis, Tunicamycin protects against LPS-induced lung injury, Pharmaceuticals 15 (2022) 134, https://doi.org/10.3390/ph15020134.

[82] L. Du, J. Zhang, X. Zhang, C. Li, Q. Wang, G. Meng, X. Kan, J. Zhang, Y. Jia, Oxypeucedanin relieves LPS-induced acute lung injury by inhibiting the inflammation and maintaining the integrity of the lung air-blood barrier, Aging (Albany NY) 14 (2022) 6626–6641, https://doi.org/10.18632/aging.204235.

[83] Y. Kim, C.-R. Bae, D. Kim, H. Kim, S. Lee, H. Zhang, M. Noh, Y.-M. Kim, N. Mochizuki, Y.-G. Kwon, Efficacy of CU06-1004 via regulation of inflammation and endothelial permeability in LPS-induced acute lung injury, J. Inflamm. 20 (2023) 13, https://doi.org/10.1186/s12950-023-00338-x.

[84] F. Kolpakov, I. Akberdin, T. Kashapov, L. Kiselev, S. Kolmykov, Y. Kondrakhin, E. Kutumova, N. Mandrik, S. Pintus, A. Ryabova, et al., BioUML: an integrated environment for systems biology and collaborative analysis of biomedical data, Nucleic Acids Res. 47 (2019) W225–W233, https://doi.org/10.1093/nar/gkz440.

[85] F. Kolpakov, I. Akberdin, I. Kiselev, S. Kolmykov, Y. Kondrakhin, M. Kulyashov, E. Kutumova, S. Pintus, A. Ryabova, R. Sharipov, et al., BioUML—towards a universal research platform, Nucleic Acids Res. 50 (2022) W124–W131, https://doi.org/10.1093/nar/gkac286.
[86] A.C. Hindmarsh, P.N. Brown, K.E. Grant, S.L. Lee, R. Serban, D.E. Shumaker, C.S. Woodward, SUNDIALS: suite of nonlinear and differential/algebraic equation solvers, ACM Trans. Math Software 31 (2005) 363–396, https://doi.org/10.1145/1089014.1089020.
[87] T.P. Runarsson, Xin Yao stochastic ranking for constrained evolutionary optimization, IEEE Trans. Evol. Comput. 4 (2000) 284–294, https://doi.org/10.1109/4235.873238.
[88] A. Raue, C. Kreutz, T. Maiwald, J. Bachmann, M. Schilling, U. Klingmüller, J. Timmer, Structural and practical identifiability analysis of partially observed dynamical models by exploiting the profile likelihood, Bioinformatics 25 (2009) 1923–1929, https://doi.org/10.1093/bioinformatics/btp358.
[89] X.Y. Li, K. Donaldson, W. MacNEE, Lipopolysaccharide-induced alveolar epithelial permeability: the role of nitric oxide, Am. J. Respir. Crit. Care Med. 157 (1998) 1027–1033, https://doi.org/10.1164/ajrccm.157.4.9605080.
[90] Y.-Y. Zhao, X.-P. Gao, Y.D. Zhao, M.K. Mirza, R.S. Frey, V.V. Kalinichenko, I.-C. Wang, R.H. Costa, A.B. Malik, Endothelial cell–restricted disruption of FoxM1 impairs endothelial repair following LPS-induced vascular injury, J. Clin. Invest. 116 (2006) 2333–2343, https://doi.org/10.1172/JCI27154.
[91] G. Wang, X. Huang, Y. Li, K. Guo, P. Ning, Y. Zhang, PARP-1 inhibitor, DPQ, attenuates LPS-induced acute lung injury through inhibiting NF-κB-Mediated inflammatory response, PLoS One 8 (2013) e79757, https://doi.org/10.1371/journal.pone.0079757.
[92] M. Piirsalu, E. Taalberg, K. Lilleväli, L. Tian, M. Zilmer, E. Vasar, Treatment with lipopolysaccharide induces distinct changes in metabolite profile and body weight in 129Sv and Bl6 mouse strains, Front. Pharmacol. 11 (2020) 371, https://doi.org/10.3389/fphar.2020.00371.
[93] J.L. Mego, Role of thiols, pH and cathepsin D in the lysosomal catabolism of serum albumin, Biochem. J. 218 (1984) 775–783, https://doi.org/10.1042/bj2180775.
[94] U. Kragh-Hansen, Possible mechanisms by which enzymatic degradation of human serum albumin can lead to bioactive peptides and biomarkers, Front. Mol. Biosci. 5 (2018) 63, https://doi.org/10.3389/fmolb.2018.00063.
[95] K.M.K. Sand, M. Bern, J. Nilsen, H.T. Noordzij, I. Sandlie, J.T. Andersen, Unraveling the interaction between FcRn and albumin: opportunities for design of albumin-based therapeutics, Front. Immunol. 5 (2015), https://doi.org/10.3389/fimmu.2014.00682.
[96] R. Molinaro, C. Corbo, M. Livingston, M. Evangelopoulos, A. Parodi, C. Boada, M. Agostini, E. Tasciotti, Inflammation and cancer: in medio stat Nano, Curr. Med. Chem. 25 (2018) 4208–4223, https://doi.org/10.2174/0929867324666170920160030.
[97] A. Parodi, D. Kostyushev, S. Brezgin, A. Kostyusheva, T. Borodina, R. Akasov, A. Frolova, V. Chulanov, A.A. Zamyatnin, Biomimetic approaches for targeting tumor-promoting inflammation, Semin. Cancer Biol. 86 (2022) 555–567, https://doi.org/10.1016/j.semcancer.2022.04.007.